Supplementary Material

Wearable Neuroimaging: Combining and Contrasting Magnetoencephalography and Electroencephalography

Elena Boto, Zelekha A. Seedat, Niall Holmes, James Leggett, Ryan M. Hill, Gillian Roberts, Vishal Shah, T. Mark Fromhold, Karen J. Mullinger, Tim M. Tierney, Gareth R. Barnes, Richard Bowtell and Matthew J. Brookes

1. Magnetometer data

In the main manuscript we showed the data from the OPMs as a "planar" gradiometer. Figure S1 contains the results of the motor task for both of the magnetometers alongside the gradiometer results from Figure 2. Panel (a) shows beta-band (13–20 Hz) filtered responses during task (green-shaded area) and rest (pink-shaded area) blocks. Single-trial responses can also be seen in the magnetometer data. TFSs are shown in panel (b), with a clear desynchronisation followed by a rebound in both magnetometer plots as well as in the gradiometer. Panel (c) contains the trial-averaged beta-band envelopes during task (blue) and rest (red). In panel (d), bar plots containing the SNR quantifications are shown: panel (i) shows the SNR during the movement-induced beta-rebound (1.5–2.4 s), when compared against the phantom measurement. Panel (ii) shows the relative beta modulation.

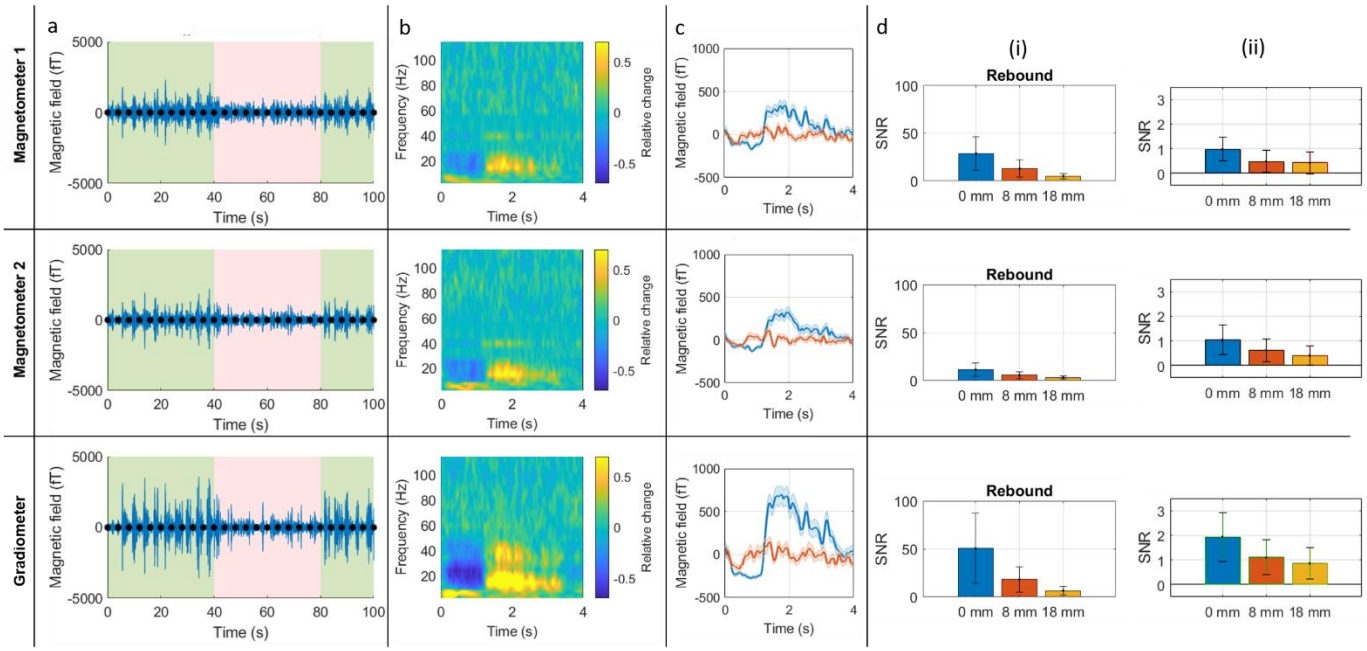

Figure S1: Beta-band responses in primary motor cortex – Magnetometer and gradiometer data. *a) Single-trial beta oscillations during task (green) and rest (pink) blocks. Black circles mark the beginning of each 4-s long trial. b) TFSs showing the oscillatory modulation across the wide band 0–110 Hz. c) Beta-band oscillatory amplitude averaged across task (blue) and rest (red) trials. d) Quantification of the (single-trial) SNR during the movement-induced beta-band rebound compared to the phantom signal (i) and based on the rest period (ii).*

Figure S2 shows resting state data acquired in both magnetometers. In both cases, the left hand plot shows OPM-magnetometer data with (purple) and without (blue) simultaneous EEG recordings. The right

hand plot shows OPM magnetometer data with (red) and without (blue) movement. Note little effect of either EEG electrodes or movement on OPM-MEG signals.

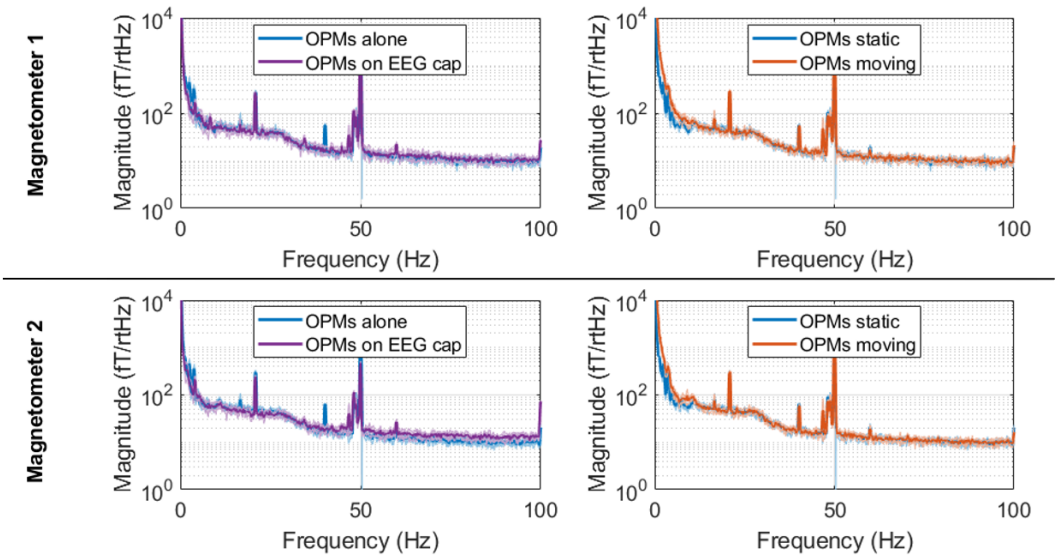

Figure S2: Concurrent EEG/MEG – resting state. *Power spectral density of the magnetometer data during resting state runs. Left plot shows magnetometer data with (purple) and without (blue) simultaneous EEG measurements. Right plots show magnetometer data while the subject kept still (blue) or moved (red).*

2. Estimating the theoretical limits on signal leakage

Assuming two dipolar sources in the brain, with amplitudes $Q_1(t)$ and $Q_2(t)$ at time t, and forward fields $\mathbf{l}_1$ and $\mathbf{l}_2$, then the MEG data, $\mathbf{m}(t)$, can be expressed mathematically as

$$\mathbf{m}(t) = \mathbf{l}_1 Q_1(t) + \mathbf{l}_2 Q_2(t) + \mathbf{e}(t), \quad [1]$$

where $\mathbf{e}(t)$ represents random noise, at time t, at the channel level. We now employ a scalar beamformer to reconstruct the source strength at some arbitrary location and orientation in the brain, represented by $\boldsymbol{\theta}$. The reconstructed source strength is given by a linear weighted sum of sensor measurements. Assuming that the weighting parameters, tuned to location and orientation $\boldsymbol{\theta}$, are $\mathbf{w}_{\boldsymbol{\theta}}$, then we write the reconstructed source amplitude as

$$\hat{Q}_{\boldsymbol{\theta}} = \mathbf{w}_{\boldsymbol{\theta}}^{\mathrm{T}} \mathbf{m}(t). \quad [2]$$

Substituting for the MEG data using Equation 1, gives

$$\hat{Q}_{\boldsymbol{\theta}} = \mathbf{w}_{\boldsymbol{\theta}}^{\mathrm{T}} \mathbf{l}_1 Q_1 + \mathbf{w}_{\boldsymbol{\theta}}^{\mathrm{T}} \mathbf{l}_2 Q_2 + \mathbf{w}_{\boldsymbol{\theta}}^{\mathrm{T}} \mathbf{e}. \quad [3]$$

Using a linearly constrained minimum variance beamformer, the weights, $\mathbf{w}_{\boldsymbol{\theta}}$, are derived based on minimisation of the variance of the output signal, with a constraint that variance originating at $\boldsymbol{\theta}$ is retained. Mathematically,

$$\min_{\mathbf{w}_{\boldsymbol{\theta}}} (E(\hat{Q}_{\boldsymbol{\theta}}^2) \text{ subject to } \mathbf{w}_{\boldsymbol{\theta}}^{\mathrm{T}} \mathbf{l}_{\boldsymbol{\theta}} = 1, \quad [4]$$

where $\mathbf{l_\theta}$ is the forward field for location and orientation $\boldsymbol{\theta}$. Note that the linear constraint ($\mathbf{w_\theta^T l_\theta} = 1$) is simply a definition of the forward field. The beamformer equation [4] can be solved analytically to generate the well-known identity

$$\mathbf{w_\theta} = \frac{\mathbf{l_\theta C^{-1}}}{\mathbf{l_\theta^T C^{-1} l_\theta}}, \quad [5]$$

where $\mathbf{C}$ represents the data covariance matrix.

We now assume that $\boldsymbol{\theta}$ is placed at the location and orientation of source 1. Assuming a perfect forward model, then $\mathbf{l_\theta} = \mathbf{l_1}$, and assuming that the noise term is orthogonal (in sensor space) to the weights (i.e. noise is negligible) we can write,

$$\hat{Q}_1 = \mathbf{w}_1^{\mathrm{T}}\mathbf{l}_1 Q_1 + \mathbf{w}_1^{\mathrm{T}}\mathbf{l}_2 Q_2. \quad [6]$$

Given that the beamformer weights are derived with the constraint that $\mathbf{w}_1^{\mathrm{T}}\mathbf{l}_1 = 1$ then, substituting for the beamformer weights, we can write

$$\hat{Q}_1 = Q_1 + \frac{\mathbf{l}_1^{\mathrm{T}}\mathbf{C}^{-1}\mathbf{l}_2}{\mathbf{l}_1^{\mathrm{T}}\mathbf{C}^{-1}\mathbf{l}_1} Q_2. \quad [7]$$

This can equivalently be written as

$$\hat{Q}_1 = Q_1 + \Delta Q_2, \quad [8]$$

where $\Delta = \frac{\mathbf{l}_1^{\mathrm{T}}\mathbf{C}^{-1}\mathbf{l}_2}{\mathbf{l}_1^{\mathrm{T}}\mathbf{C}^{-1}\mathbf{l}_1}$ represents the leakage term.

We now wish to calculate the magnitude of Δ, and to do this we must first compute a mathematical form for the data covariance, $\mathbf{C}$. Assuming that our two dipole time courses are temporally uncorrelated, then we can write

$$\mathbf{C} = Q_1^2\mathbf{l}_1\mathbf{l}_1^{\mathbf{T}} + Q_2^2\mathbf{l}_2\mathbf{l}_2^{\mathbf{T}} + v^2\mathbf{I}, \quad [9]$$

where $v^2\mathbf{I}$ represents uncorrelated sensor noise. The form of this Equation means that the inverse of the covariance, $\mathbf{C}^{-1}$, can be calculated using the Sherman-Morrison-Woodbury matrix inversion Lemma. Specifically,

$$\mathbf{C}^{-1} = \frac{1}{v^2}\left[\mathbf{I} - \frac{1}{1 - f_1 f_2 \cos^2(\lambda_{12})}\left\{f_1 \frac{\mathbf{l}_1\mathbf{l}_1^{\mathrm{T}}}{\|\mathbf{l}_1\|_{\mathrm{F}}^2} + f_2 \frac{\mathbf{l}_2\mathbf{l}_2^{\mathrm{T}}}{\|\mathbf{l}_2\|_{\mathrm{F}}^2} - f_1 f_2 \cos(\lambda_{12}) \frac{\mathbf{l}_2\mathbf{l}_1^{\mathrm{T}} + \mathbf{l}_1\mathbf{l}_2^{\mathrm{T}}}{\|\mathbf{l}_1\|_{\mathrm{F}}\,\|\mathbf{l}_2\|_{\mathrm{F}}}\right\}\right], \quad [10]$$

where

$$f_1 = \frac{Q_1^2\|\mathbf{l}_1\|_{\mathrm{F}}^2}{v^2 + Q_1^2\|\mathbf{l}_1\|_{\mathrm{F}}^2} \quad [11]$$

and

$$f_2 = \frac{Q_2^2\|\mathbf{l}_2\|_{\mathrm{F}}^2}{v^2 + Q_2^2\|\mathbf{l}_2\|_{\mathrm{F}}^2}. \quad [12]$$

The subscript 'F' indicates a Frobenius norm. The angle, λ_{12}, is given by the dot product of the forward fields of the two sources; mathematically,

$$\mathbf{l}_1^{\mathrm{T}}\mathbf{l}_2 = \|\mathbf{l}_1\|\|\mathbf{l}_2\|\cos(\lambda_{12}). \quad [13]$$

It is also noteworthy that, from Equation 13, the quantity $\cos(\lambda_{12})$ is equivalent to the Pearson product moment correlation coefficient between $\mathbf{l}_1$ and $\mathbf{l}_2$, and for this reason we let

$$R_{12} = \cos(\lambda_{12}). \quad [14]$$

Defining $P_1 = \frac{1}{\mathbf{l}_1^{\mathrm{T}}\mathbf{C}^{-1}\mathbf{l}_1}$ (which represents the beamformer-projected power for source 1), and by comparison of Equations 7 and 8, we can write

$$\Delta = P_1\mathbf{l}_1^{\mathrm{T}}\mathbf{C}^{-1}\mathbf{l}_2. \quad [15]$$

Substituting into Equation 9, we find

$$\delta = \frac{P_1}{\nu^2}\left[\mathbf{l}_1^{\mathrm{T}}\mathbf{l}_2 - \frac{1}{1-f_1f_2R_{12}}\left\{f_1\frac{\mathbf{l}_1^{\mathrm{T}}\mathbf{l}_1\mathbf{l}_1^{\mathrm{T}}\mathbf{l}_2}{\|\mathbf{l}_1\|_{\mathrm{F}}^2} + f_2\frac{\mathbf{l}_1^{\mathrm{T}}\mathbf{l}_2\mathbf{l}_2^{\mathrm{T}}\mathbf{l}_2}{\|\mathbf{l}_2\|_{\mathrm{F}}^2} - f_1f_2R_{12}\frac{\mathbf{l}_1^{\mathrm{T}}\mathbf{l}_2\mathbf{l}_1^{\mathrm{T}}\mathbf{l}_2+\mathbf{l}_1^{\mathrm{T}}\mathbf{l}_1\mathbf{l}_2^{\mathrm{T}}\mathbf{l}_2}{\|\mathbf{l}_1\|_{\mathrm{F}}\ \|\mathbf{l}_2\|_{\mathrm{F}}}\right\}\right] \quad [16]$$

and rearranging and simplifying this expression, produces a solution for the leakage, Δ, given by

$$\Delta = \frac{P_1\|\mathbf{l}_1\|_{\mathrm{F}}\|\mathbf{l}_2\|_{\mathrm{F}}}{\nu^2}\left[\frac{R_{12}(1-(f_1+f_2)+f_1f_2)}{1-f_1f_2R_{12}^2}\right]. \quad [17]$$

However, we need to recognise that $P_1 = \frac{1}{\mathbf{l}_1^{\mathrm{T}}\mathbf{C}^{-1}\mathbf{l}_1}$; in other words, P_1 is also a function of the inverse covariance. Specifically, we can write,

$$P_1^{-1} = \frac{1}{\nu^2}\left[\boldsymbol{l}_1^T\boldsymbol{l}_1 - \frac{1}{1-f_1f_2R_{12}^2}\left\{f_1\frac{\boldsymbol{l}_1^T\boldsymbol{l}_1\boldsymbol{l}_1^T\boldsymbol{l}_1}{\|\boldsymbol{l}_1\|_F^2} + f_2\frac{\boldsymbol{l}_1^T\boldsymbol{l}_2\boldsymbol{l}_2^T\boldsymbol{l}_1}{\|\boldsymbol{l}_2\|_F^2} - f_1f_2R_{12}\frac{\boldsymbol{l}_1^T\boldsymbol{l}_2\boldsymbol{l}_1^T\boldsymbol{l}_1+\boldsymbol{l}_1^T\boldsymbol{l}_1\boldsymbol{l}_2^T\boldsymbol{l}_1}{\|\boldsymbol{l}_1\|_F\|\boldsymbol{l}_2\|_F}\right\}\right], \quad [18]$$

which simplifies to

$$P_1^{-1} = \frac{\|\mathbf{l}_1\|_{\mathrm{F}}^2}{\nu^2}\left[\frac{1-f_1+(f_1f_2-f_2)R_{12}^2}{(1-f_1f_2R_{12}^2)}\right]. \quad [19]$$

Combining Equations 17 and 19 we obtain

$$\Delta = \frac{\nu^2}{\|\boldsymbol{l}_1\|_F^2}\left[\frac{(1-f_1f_2R_{12}^2)}{1-f_1+(f_1f_2-f_2)R_{12}^2}\right]\frac{\|\mathbf{l}_1\|_{\mathrm{F}}\|\mathbf{l}_2\|_{\mathrm{F}}}{\nu^2}\left[\frac{R_{12}(1-(f_1+f_2)+f_1f_2)}{1-f_1f_2R_{12}^2}\right], \quad [20]$$

which simplifies to a final expression for the leakage magnitude,

$$\Delta = \frac{\|\mathbf{l}_2\|_{\mathrm{F}}}{\|\mathbf{l}_1\|_{\mathrm{F}}}\left[\frac{R_{12}(1-(f_1+f_2)+f_1f_2)}{1-f_1+(f_1f_2-f_2)R_{12}^2}\right]. \quad [21]$$

This expression is used in the simulations to provide a quantitative estimate of the spatial selectivity of the beamformer. As noted in the main manuscript, the critical parameters are R_{12}, the correlation of forward field topographies, and f_1 and f_2, the normalised SNRs of the two sources. It proves instructive to examine the behaviour of Δ as a function of R_{12}; further simplifying Equation 21, by assuming that the two sources have approximately equal magnitude and depth in the brain, such that $\|\mathbf{l}_1\|_{\mathrm{F}} \approx \|\mathbf{l}_2\|_{\mathrm{F}}$ and $f_1 \approx f_2 \approx f$, we can write

$$\Delta \approx \frac{r_{12}(1-2f+f^2)}{1-f+(f^2-f)R_{12}^2}. \quad [22]$$

Figure S3 shows Δ plotted against R_{12}, in accordance with Equation 22, for a number of different values of the SNR. Note that, for low SNR sources, the leakage is almost a linear function of the forward field correlation. However, at higher SNR values, the beamformer is able to separate the sources clearly (Δ is low) even in the case where the forward fields look relatively similar.

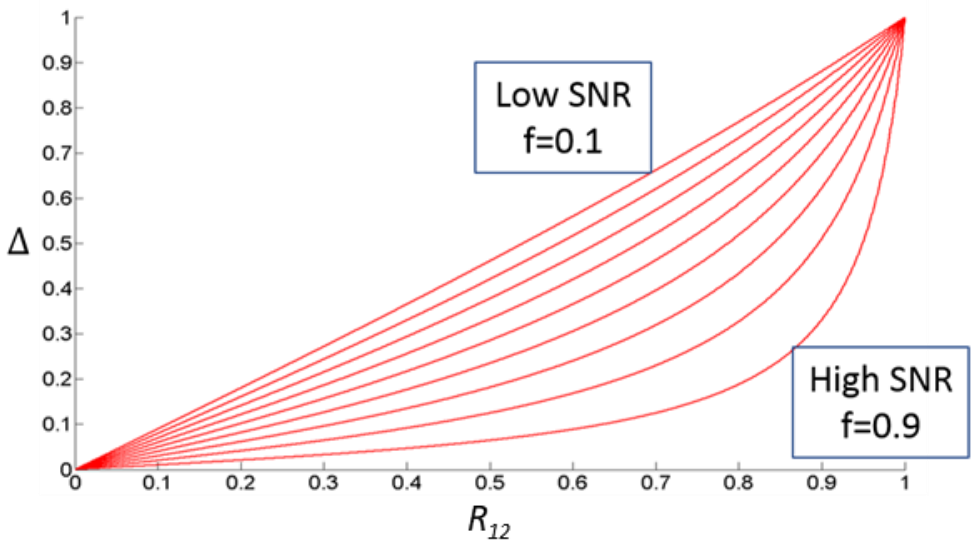

Figure S3: *Variation of beamformer source leakage, Δ, with correlation between source topographies, R_{12}. Several curves are shown representing SNR values ranging from 0.1 to 0.9 in steps of 0.1.*

3. *Supplementary simulation results*

In the main manuscript we showed simulation results for EEG and OPM-MEG. However, for completeness, our simulation also took into account a cryogenic MEG device, where we assumed that the pick-up coils were located ~2.5 cm from the scalp. Figure S4 is equivalent to Figure 8a in the manuscript, but with the addition of the cryogenic MEG system. Note the larger radius sphere representing the fact that the sensors are further from the scalp. The increased spatial diffusivity of measured field patterns for cryogenic, (compared to OPM) MEG is clear, and this effectively leads to reduced spatial degrees of freedom in the extracranial measurements.

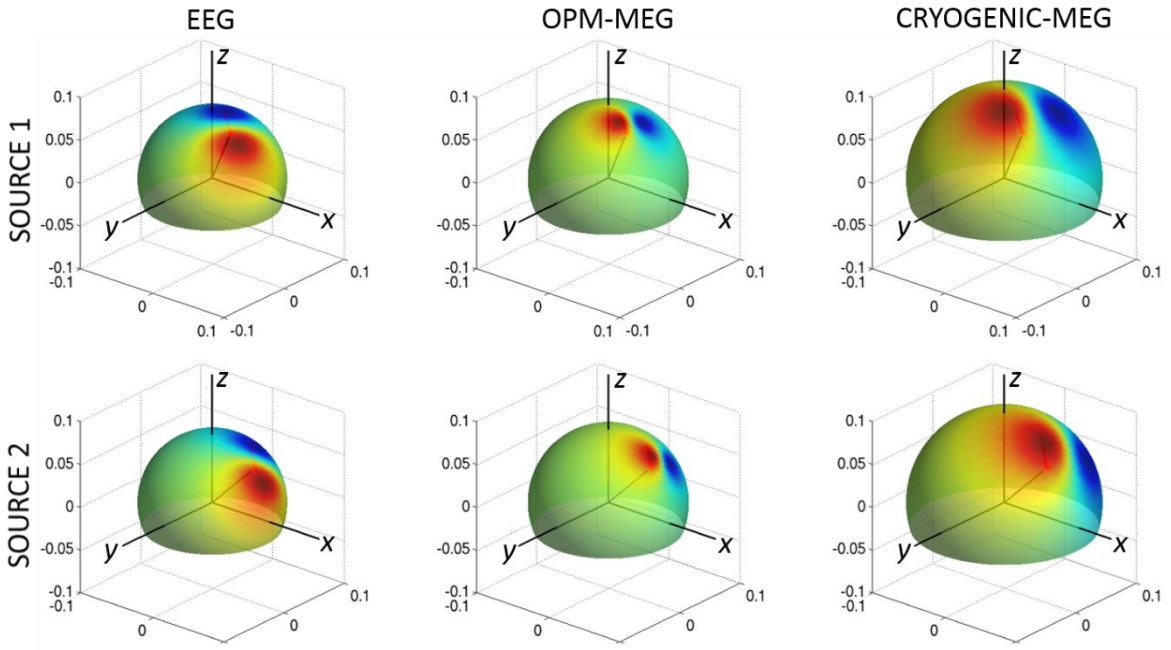

Figure S4: Example field patterns from two sources. *Fields are simulated for EEG (left) OPM-MEG (centre) and cryogenic MEG (right). This is equivalent to Figure 8a in the main manuscript but with the addition of cryogenic MEG. In EEG, field patterns are made diffuse by the low conductivity of the skull; in cryogenic MEG, field patterns are made diffuse by the proximity of the sensors. In OPM-MEG however, field patterns contain higher spatial frequencies on the sphere surface.*

We assumed a random noise level of 10fT/sqrt(Hz) for OPM-MEG, 5 fT/ sqrt(Hz) for cryogenic MEG, and 120nV/sqrt(Hz) for EEG; we also assumed a bandwidth of 100Hz giving overall noise amplitudes of 100 fT, 50 fT and 1.2 μV. Figure S5, upper panel, shows the signal-to-noise ratios (here measured as the absolute amplitude of the maximum value in the lead field divided by the noise) as a function of source depth from the brain surface, and orientation angle with respect to the radial direction. As expected, both modalities have highest SNR for shallow sources. MEG is advantageous for tangentially oriented dipoles whilst EEG is best for radial sources. Note that our simulated noise levels are such that the SNR for EEG (for a radial source) is approximately the same as that for conventional MEG (for a tangential source).

Figure S5, also shows forward field correlation, R_{12} (centre panel) and estimated leakage, Δ (lower panel) plotted as a function of source separation and depth in the brain. As described in our main paper, low values (i.e. more blue) of both R_{12} and Δ are desirable as they indicate improved spatial resolution. We see that R_{12} for EEG and conventional MEG are approximately the same whereas OPM-MEG offers fundamental advantages due to more spatially focal field patterns. When looking at leakage (which not only takes into account spatial resolution but also signal-to-noise ratio, again we see OPMs have an advantage over EEG and conventional MEG with generally lower leakage values. Conventional MEG is also shown to be advantageous over EEG however this is a result of the simulation parameters which used tangential sources (see below).

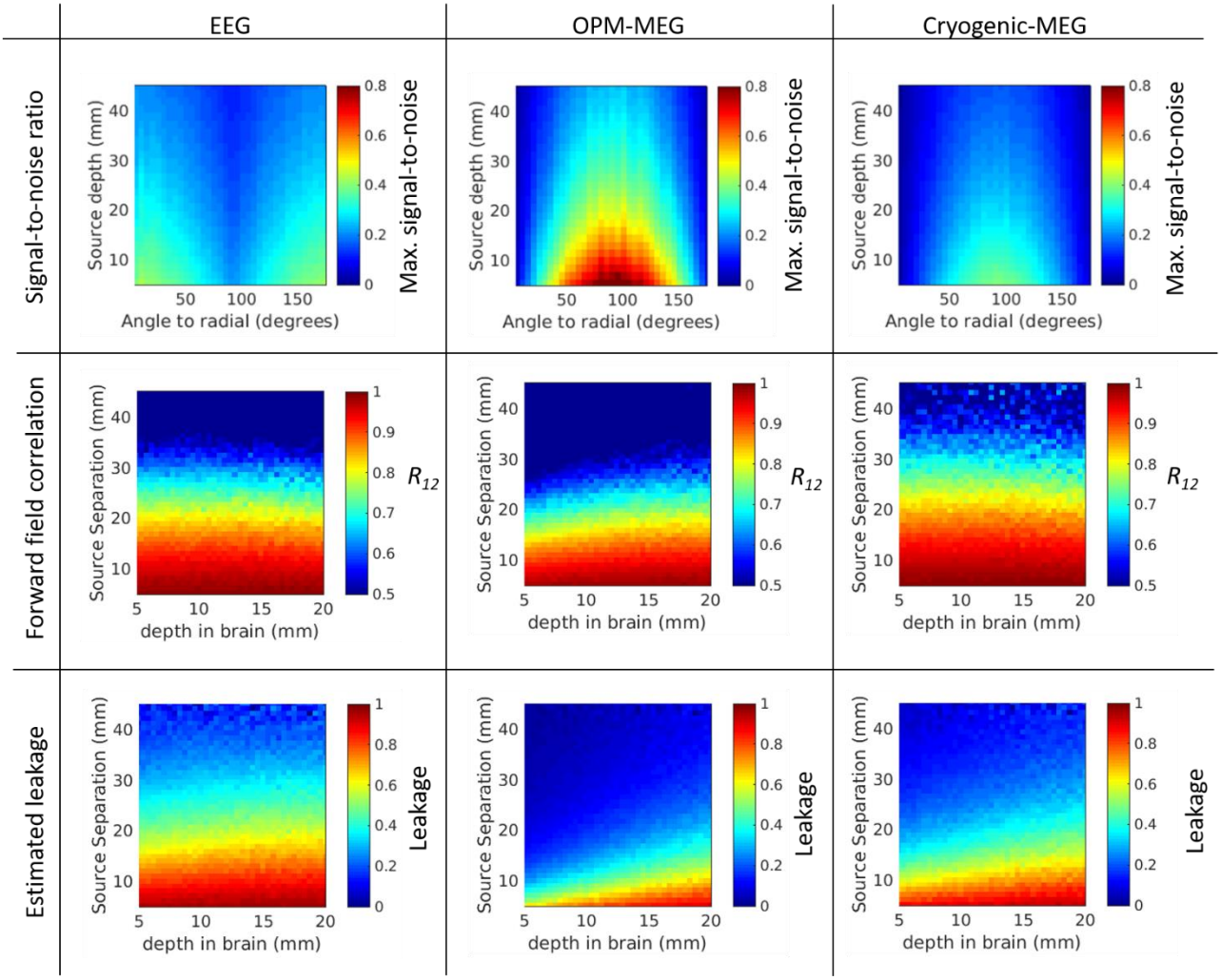

Figure S5: Equivalent results to Figure 8c/d but with conventional MEG included. Upper panel shows *Parametric* ***variation of SNR (maximum lead field divided by noise), centre and lower panels shows*** *variation of spatial correlation of forward fields and source leakage respectively. All are shown plotted against source separation and source depth, for EEG, OPM-MEG and conventional MEG.*

Figure S6 shows forward field correlation, R_{12}, (upper six plots) and leakage (lower six plots), plotted against source orientation and the direction of source separation. In both cases the upper panel shows the raw values of R_{12} and Δ, whereas the lower panels show which modality is advantageous. The complementary nature of EEG and MEG are shown clearly; e.g. comparing EEG and cryogenic MEG, we see that when the direction of source separation is parallel to the source orientation ($\phi \to 0^o$ or $\phi \to 180^o$), EEG offers better spatial specificity; when the direction of source separation is perpendicular to the source orientation ($\phi \to 90^o$), MEG offers better spatial specificity. Further, we see that for radial sources (to which MEG is insensitive) EEG also offers advantages as would be expected. It is these complementarities which have been the source of a large body of literature showing the advantages of concurrent MEG/EEG. However, for OPM-MEG, the fundamental improvement in spatial resolution means that, in the vast majority of cases, OPM-MEG offers lower leakage than EEG – the exception being when sources are very close to radial. This leads us to believe that concurrent EEG/MEG bight be less beneficial (from a spatial resolution point of view) for OPM-MEG than for cryogenic MEG.

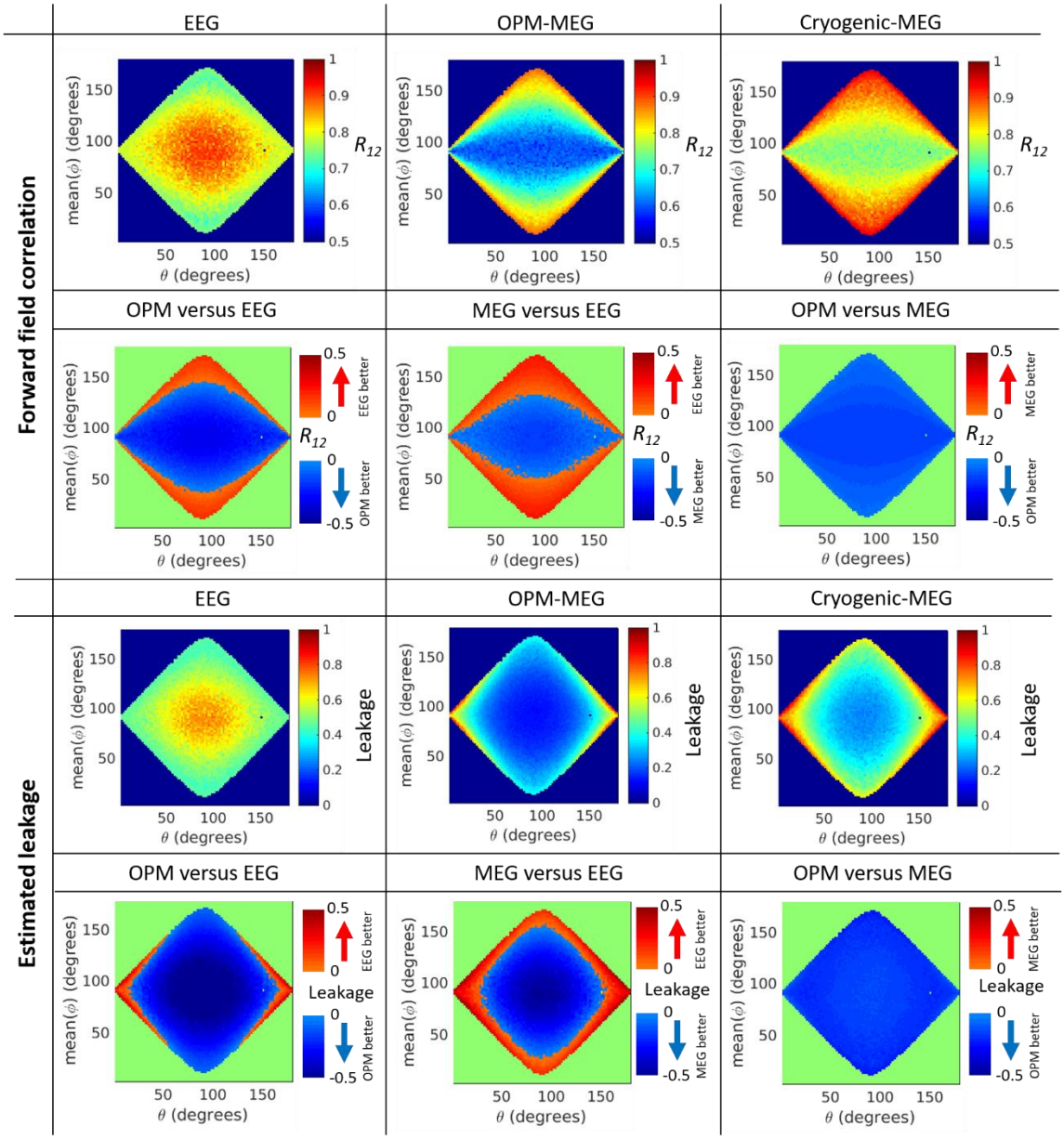

Figure S6: Equivalent results to Figure 8c/d but with conventional MEG included. *Parametric variation of spatial correlation of forward fields (upper plots) and source leakage (lower plots) are shown plotted against source orientation and the direction of source separation, for EEG, OPM-MEG and conventional MEG.*

We stress that these simulations have limitations. We are using simple forward models (based on spherical approximations). In particular, the model used for EEG – which involves a triple concentric sphere and literature-based values for conductivity and skull thickness – is an over-simplification of the highly complex morphology of conductivity in a real head. Indeed, even the conductivity of the skull is still a matter for debate in the literature: the values that we have used (a ratio of ~1/80 for brain-scalp/skull) are in line with those most commonly used, but other literature suggests that the conductivity of the skull could be higher. Further, we have taken only representative noise values (given the known susceptibility of EEG to biological artefact, the values taken for EEG are likely underestimates). We have also assumed that the sensors are placed on a spherical surface, and we have not taken into account known brain structure (i.e. that dipoles are oriented perpendicular to the cortical sheet). Nevertheless, these results illustrate that, given a straightforward physical model of electric potentials and magnetic fields generated in the brain, OPMs offer fundamental advantages when reconstructing underlying brain current distributions.